TOPICAL REVIEW

Moiré and beyond in transition metal dichalcogenide twisted bilayers

To cite this article: Kha Tran *et al* 2021 *2D Mater.* **8** 022002

View the article online for updates and enhancements.

You may also like

2D Materials

TOPICAL REVIEW

Moiré and beyond in transition metal dichalcogenide twisted bilayers

Kha Tran[1], Junho Choi[2] and Akshay Singh[3]

1 NRC research associate at the Naval Research Laboratory, 4555 Overlook Ave SW, Washington, DC 20375, United States of America
2 Department of Physics, The University of Texas at Austin, Austin, TX 78712, United States of America
3 Department of Physics, Indian Institute of Science, Bengaluru, Karnataka 560012, India

E-mail: kha.tran.ctr@nrl.navy.mil and aksy@iisc.ac.in

Abstract

Fabricating van der Waals bilayer heterostructures (BL-HS) by stacking the same or different two-dimensional layers, offers a unique physical system with rich electronic and optical properties. Twist-angle between component layers has emerged as a remarkable parameter that can control the period of lateral confinement, and nature of the exciton (Coulomb bound electron–hole pair) in reciprocal space thus creating exotic physical states including moiré excitons (MXs). In this review article, we focus on opto-electronic properties of excitons in transition metal dichalcogenide semiconductor twisted BL-HS. We look at existing evidence of MXs in localized and strongly correlated states, and at nanoscale mapping of moiré superlattice and lattice-reconstruction. This review will be helpful in guiding the community as well as motivating work in areas such as near-field optical measurements and controlling the creation of novel physical states.

1. Introduction

The scientific community has witnessed tremendous work in the semiconducting two-dimensional (2D)-transition metal dichalcogenide (TMD) layered materials space in the past 10 years. In the spirit of the facile equation 2D + 2D = 2D, significant progress has been made in fabricating van der Waals (vdW) bilayer heterostructures (BL-HS) by stacking the same or different component layers [1–3]. Such a BL-HS has many degrees of freedom including layer composition, physical nature (metallic, semiconducting), method of preparation, twist-angle and stacking order. Through a combination of these degrees of freedom, new applications towards quantum information, opto-electronic transport and integrated-photonics are expected [4–7].

Quantum information has advanced from a strictly-academic to an industrially-relevant endeavor, with recent work claiming quantum supremacy in the case of certain algorithms [8]. However, to create scalable computing and communication systems, there is a critical need of reliable, environmentally-protected and deterministically-located solid-state single photon sources. In parallel,

there is an increased focus on integration of advanced 2D nanomaterials in traditional electronic circuits, and to understand and control electronic and thermal transport. For example, by interfacing various 2D materials, ultra-high thermal insulation has been observed, which can be exploited for thermal management and energy harvesting [9].

Twisted BL-HS offers novel control over opto-electronic properties, via control of periodicity and correlations. Analogous to twisting two polarizer sheets to control transmission of light, twisted BL-HS can control optical and electronic transport. Additionally, like taking a picture of a pixelated screen, an emergent moiré structure with beautiful patterns and high symmetry points offers a new super-structure. In practice, for BL-HS, tunable twist-angle leads to modification of reciprocal space, momentum mismatch, change of interlayer spacing, Coulomb interactions and tunable correlations.

Moiré superlattices can form when two monolayers (MLs) having slightly different lattice constant and/or finite twist-angle are stacked vertically. Figure 1 center panel shows a schematic of the moiré superlattice in BL-HS with different twist angles. The unit cell of moiré superlattice is the moiré supercell.

The size of the supercell a_M, as a function of twist-angle θ is given by [10]

$$a_M = \frac{(1+\delta)\,a_0}{\sqrt{2\,(1+\delta)\,(1-\cos\theta)+\delta^2}},$$

where δ is the lattice mismatch defined as $|a'_0 - a_0|/a_0$; a_0 and a'_0 are the lattice constants of the two constituent MLs ($a_0 < a'_0$). For near-zero twist-angle in a small lattice mismatch BL-HS, size of the moiré supercell can be quite large i.e. tens of nanometers as compared to Bohr radius of the exciton (few nanometers). Thus, the exciton can be described as a particle moving in a slowly varying moiré potential [11, 12].

There are several questions that the 2D materials twistronics community has endeavored to answer in the recent years. How are optical properties of an exciton modified in the presence of another layer, beyond a simple dielectric environment change? Can we have reliable single photon emitters in 2D materials? Can component layers be considered as separate layers, or as a vdW solid? Can spin-valley coupling result in novel physics in BL-HS? We have strived to examine possible answers and have organized this review to cover fundamental and application-relevant concepts in twisted TMD BL-HS. We briefly discuss HS preparation, especially focusing on controlling and measuring twist. Figure 1 lays out the scheme in which our review is structured. We review properties of interlayer excitons (IELXs), intralayer excitons (IALXs), and hybridized excitons (HXs) modulated by the moiré potential. We examine the effect of moiré superlattice on exciton diffusion, as well as discuss possibilities of investigating Hubbard model physics and measuring strongly correlated states. We finally review the possibility of reconstruction in small twist-angle BL-HS, which goes beyond the rigid moiré superlattice picture.

2. Twisted bilayer-heterostructure (BL-HS) preparation

Since a number of review papers have already discussed the basics of TMD BL-HS preparation, we will not strive to cover all aspects of HS preparation [1, 3]. We only focus on methods to control the twist (azimuthal angle) between component MLs of a BL-HS. We note that sequential preparation of a twisted BL-HS using chemical vapor deposition (CVD) is not possible for small twist-angles <2–5°. This is because the layers conformally grow, and can undergo lattice expansion (or contraction) for epitaxial or thermodynamically favorable-orientation growth [13].

Therefore, the dominant and most suitable method for twist-controlled BL-HS preparation is sequential mechanical stacking of exfoliated or CVD-synthesized MLs using dry [14, 15] or wet transfer methods [1, 3, 16, 17]. Since encapsulation by hexagonal-boron nitride (hBN) improves
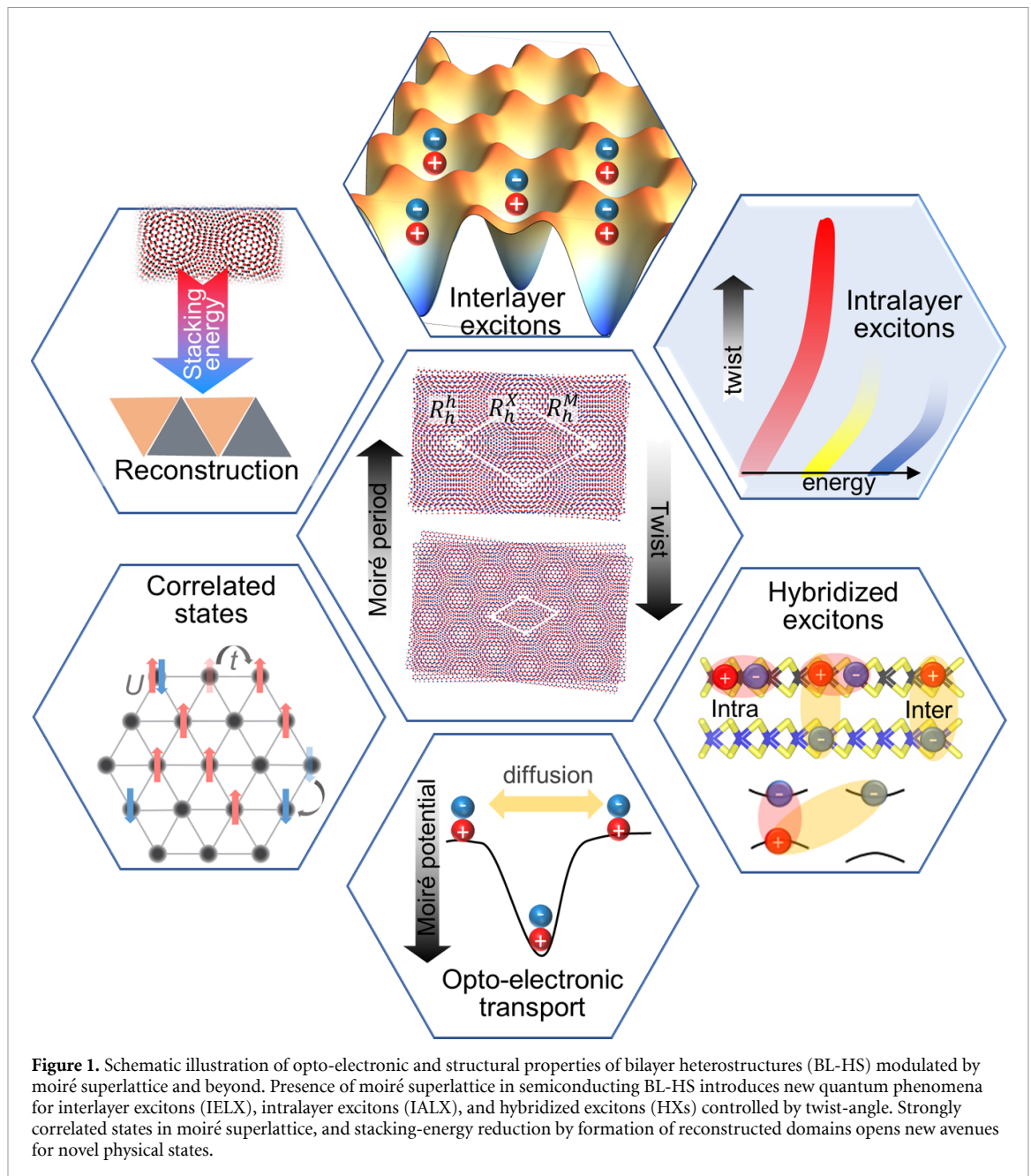
opto-electronic properties, including narrowing of linewidths and reducing surface charge, we will introduce how to fabricate an hBN encapsulated BL-HS by the dry transfer technique [14, 18]. Briefly, a polymer mask contacts the top hBN layer (exfoliated on a silicon or polymer substrate) at an elevated temperature. The top hBN layer is picked up, then TMD ML1, then ML2 and finally the bottom hBN. The encapsulated BL-HS drops onto a substrate upon contact and heating (to temperature beyond the polymer softening temperature). A solvent step follows to remove any polymer residue, followed by annealing in vacuum or inert conditions.

Coarse control of twist-angle during stacking is provided via straight-edge of CVD ML or fracture/tear along a crystal orientation (zigzag or armchair) for mechanically exfoliated ML. Orientation of the constituent MLs is determined before stacking by measuring second harmonic generation, and twist-angle alignment is performed accordingly. In this way, the relative twist can be controlled with an accuracy of ∼0.5–1° [19, 20]. Geometric guidance can serve to improve the angle accuracy to better than 1° by using larger crystals [21]. This technique was recently extended to centimeter scale HS [22]. For preparing homo BL-HS, mechanical tearing of part of the ML, rotation, and subsequent stacking back (on the parent ML) can be applied for high accuracy ∼0.2° [15, 23]. An alternative is preparing an upper rotatable layer, and rotation with a microscopic tip [10].

3. Opto-electronic properties of moiré excitons in twisted TMD BL-HS

Throughout this review, we denote the parallel (anti-parallel) stacking near 0° (60°) twist-angle as R-type (H-type). Within the moiré supercell, there are three locations R_h^h, R_h^X, and R_h^M (H_h^h, H_h^X, and H_h^M) in which the three-fold rotational symmetry is preserved (figure 1 center panel). R_h (H_h^μ) refers to R-type (H-type) stacking with the μ site (h—hexagonal center, X—chalcogen atom, M—metal atom) of the top layer aligning with the hexagonal center (h) of the bottom layer [11, 24].

Further, due to different band gap and the work function of two constituent MLs, TMD BL-HS can have type-II band alignment [25–27]. Both IALX (electron and hole in the same layer) and IELX (electron and hole in different layers) can be present. IELX has much weaker optical dipole moment than that of IALX, and has much longer lifetime due to the spatial separation of electron and hole [26, 28–30]. In the simplest case with zero twist-angle, the bandgap is direct, giving rise to direct momentum IELX. As the twist-angle increases, the conduction band (CB) minimum moves away from the valence band (VB) maximum at K point [31]. The IELX becomes indirect in momentum space with decreasing dipole moment,

Figure 1. Schematic illustration of opto-electronic and structural properties of bilayer heterostructures (BL-HS) modulated by moiré superlattice and beyond. Presence of moiré superlattice in semiconducting BL-HS introduces new quantum phenomena for interlayer excitons (IELX), intralayer excitons (IALX), and hybridized excitons (HXs) controlled by twist-angle. Strongly correlated states in moiré superlattice, and stacking-energy reduction by formation of reconstructed domains opens new avenues for novel physical states.

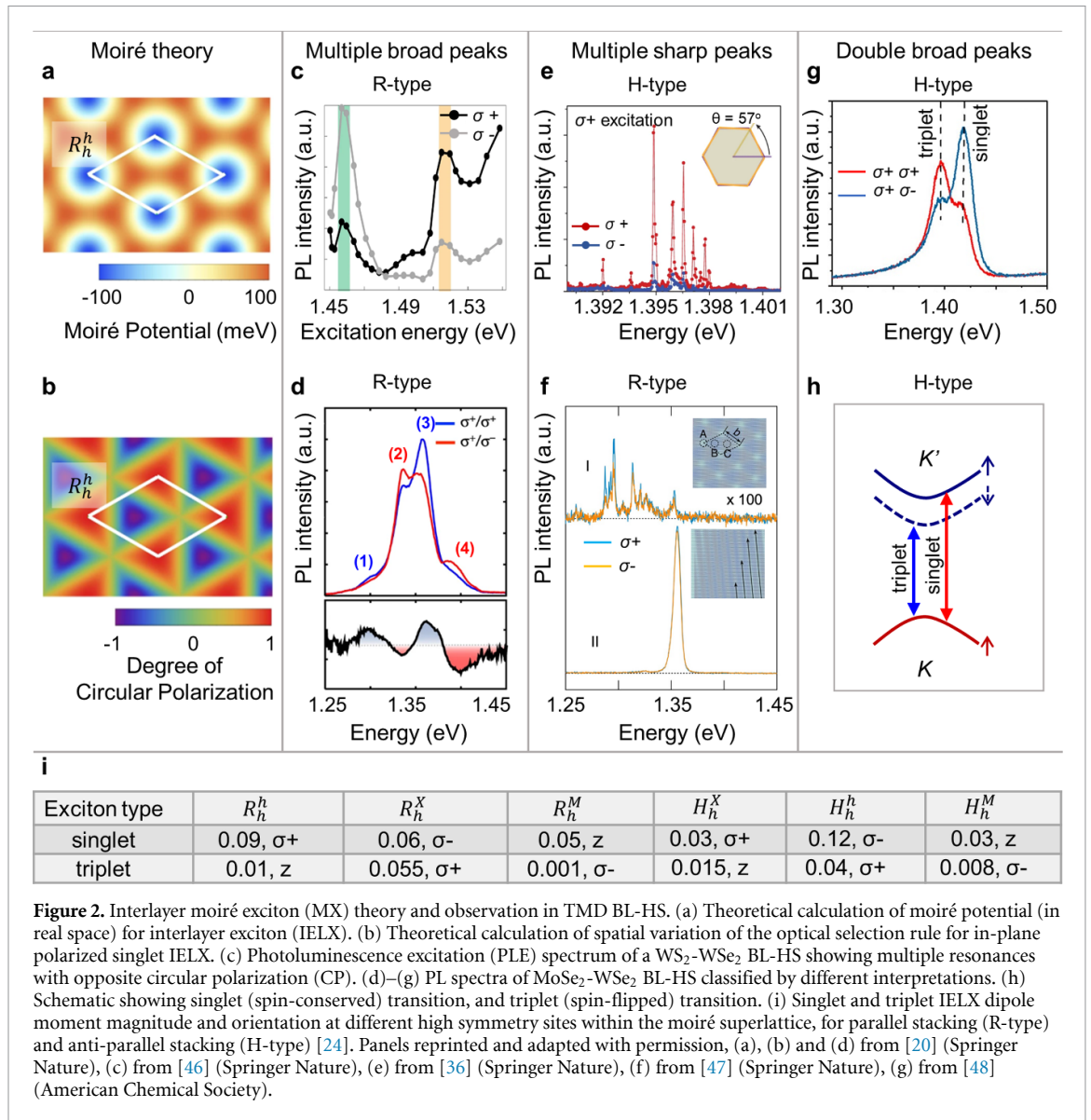decreasing emission intensity [32, 33] and increasing the lifetime [34].

As we will see in the following sections, moiré superlattice changes the optical and electronic properties of IELX and IALX drastically. It can localize excitons and lead to spatial variation of optical selection rules in IELXs [11, 20, 35, 36], form topological exciton bands leading to additional satellite IALX peaks [19, 37], and form triangular lattice Hubbard models for electrons or holes that simulate strong-correlation physics [38–41].

4. Interlayer moiré excitons

Moiré superlattice imposes a periodic potential on the IELX. In a study of a rotationally aligned MoS_2-WSe_2 BL-HS [42], the local bandgap spatial variation was directly correlated with the local atomic alignment of the two MLs. The bandgap is modulated with a potential depth of $\sim$150 meV in the lateral direction. The local maxima and minima of bandgap coincide with high symmetry sites of the moiré superlattice (figure 2(a)). Therefore, multiple IELX resonances are expected to form due to the moiré lateral confinement [43, 44]. The moiré potential is strongest ($\sim$150 meV) near 0° twist-angle (R-type), and is estimated to be much weaker $\sim$10–20 meV near 60° (H-type) [12, 35, 45]. 2D array of identical quantum emitters is expected to form in a deep moiré potential with a long moiré superlattice period [11].

Unlike the IALX, both the spin-conserved (singlet) and spin-flip (triplet) IELXs can couple to in-plane and out-of-plane polarized light (figures 2(h)

Figure 2. Interlayer moiré exciton (MX) theory and observation in TMD BL-HS. (a) Theoretical calculation of moiré potential (in real space) for interlayer exciton (IELX). (b) Theoretical calculation of spatial variation of the optical selection rule for in-plane polarized singlet IELX. (c) Photoluminescence excitation (PLE) spectrum of a WS$_2$-WSe$_2$ BL-HS showing multiple resonances with opposite circular polarization (CP). (d)–(g) PL spectra of MoSe$_2$-WSe$_2$ BL-HS classified by different interpretations. (h) Schematic showing singlet (spin-conserved) transition, and triplet (spin-flipped) transition. (i) Singlet and triplet IELX dipole moment magnitude and orientation at different high symmetry sites within the moiré superlattice, for parallel stacking (R-type) and anti-parallel stacking (H-type) [24]. Panels reprinted and adapted with permission, (a), (b) and (d) from [20] (Springer Nature), (c) from [46] (Springer Nature), (e) from [36] (Springer Nature), (f) from [47] (Springer Nature), (g) from [48] (American Chemical Society).

and (i)) due to breaking of the out-of-plane mirror symmetry [24]. This relaxation of spin selection rule described by Yu *et al* [24] consequently results in comparable transition dipole moments for singlet and triplet IELXs, which can then be equally bright in an optical measurement.

Moiré superlattice imposes a spatial variation of optical selection rules on both spin-singlet and spin-triplet IELX. The optical dipole moment can point either in-plane (σ_+/σ_- polarizations) or out-of-plane (z polarization) depending on where the IELX is located within the moiré superlattice [24]. Only at the three-fold symmetry sites, the IELX is fully circular or out-of-plane polarized; selection rules are summarized in figure 2(i) for 0° and 60° twist-angles. In between these sites, the selection rules vary continuously within the moiré supercell [24]. Figure 2(b) maps spatial variation of the in-plane degree of circular polarization (CP) $(\sigma_+ - \sigma_-)/(\sigma_+ + \sigma_-)$, for the spin-singlet IELX. The selection rules of interlayer moiré excitons (MXs) are few of many important

clues for understanding the physical origin of MXs, as we see below.

The main difficulty of finding direct evidence for interlayer MXs in optical experiments is due to limited spatial resolution. Within a laser spot size (~1 μm), there are thousands of moiré supercells, so the effect of inhomogeneous broadening (due to strain and impurities) on measured optical properties is unavoidable. Nevertheless, various research groups have relied on other clues (for example, spectral resolution, CP, g-factor) to support their claim of interlayer MX observation. Although studying the similar HS, mainly hBN encapsulated MoSe$_2$-WSe$_2$ HS, the optical results and interpretations vary vastly across different research groups. Below, we attempt to classify these studies based on the similarity of their main results and interpretations.

4.1. Broad peaks with alternating/opposite CP
Tran *et al* [20] have reported multiple IELX resonances in photoluminescence (PL) measurements of

hBN encapsulated MoSe$_2$-WSe$_2$ BL-HS at low temperature. These peaks are attributed to the ground state and excited states of singlet IELXs, all confined in the moiré potential at site R_h^h. Analogous to the hydrogen atom, ground state (lowest energy peak) IELX has s-like wavefunction. The next higher energy resonance has p-like wavefunction, and so on (d-like, f-like). The IELXs inherit the valley selection rule based on the spatial distribution of their wavefunctions within the moiré superlattice [11]. The peak (1) with lowest energy has s-wave symmetry centered at the R_h^h site, and its optical matrix element has σ_+ component only. The peak (2) has chiral p-wave form with an additional angular momentum, and thus mainly has σ_- component. Similar behaviors can be inferred for peaks (3) and (4) [35]. Consequently, these peaks exhibit alternating selection rules upon PL emission (figure 2(d)). The attribution of interlayer MX to spin-triplet interlayer resonances are ruled out based on the temperature dependence and PL lifetime measurements.

Jin *et al* [46] have reported multiple IELX resonances in hBN encapsulated WS$_2$-WSe$_2$ BL-HS at near zero twist-angle. Although PL measurements only reveal one IELX peak at 1.43 eV, PL excitation (figure 2(c)) and resonant pump-probe measurements show the emergence of two higher energy IELX peaks (1.46 eV and 1.51 eV) with opposite CP. Their oscillator strengths are revealed directly by the pump-probe measurement and are 100 times smaller than the IALX transitions. Due to the energy separation, CP, and relative oscillator strengths among IELX peaks, 1.43 eV and 1.46 eV peaks are attributed to spin-triplet and spin-singlet transitions localized at R_h^X site respectively; 1.51 eV peak is attributed to the spin-singlet transition at R_h^h site. Spin-triplet transition at site R_h^h is not observed.

4.2. Sharp peaks with uniform CP

Numerous studies have reported moiré potential trapped IELXs with very sharp linewidth ∼100 μeV measured by PL at low excitation power (tens of nanowatts) [36, 47, 49–51]. The resonances span approximately 100 meV, and are attributed to excitons trapped in the moiré potential because of their sharp linewidth and their uniform g-factor, −16 for anti-parallel stacking (7 for parallel stacking) which is similar to the inhomogeneously broadened free IELX broad peak [36, 49, 50]. Interestingly, under circularly polarized excitation, all the peaks exhibit uniform CP either all negative or all positive, depending on the twist-angle, suggesting similar physical origin within the moiré superlattice[36] (figures 2(e) and (f)). Baek *et al* [49]. provides evidence of photon antibunching nature of the moiré trapped IELX in an anti-parallel stacked MoSe$_2$-WSe$_2$ BL-HS by measuring coincidence value g^2(0) below 0.5. Moreover, an out-of-plane electric field can tune these quantum emitters up to 40 meV [49], suggesting the possibility
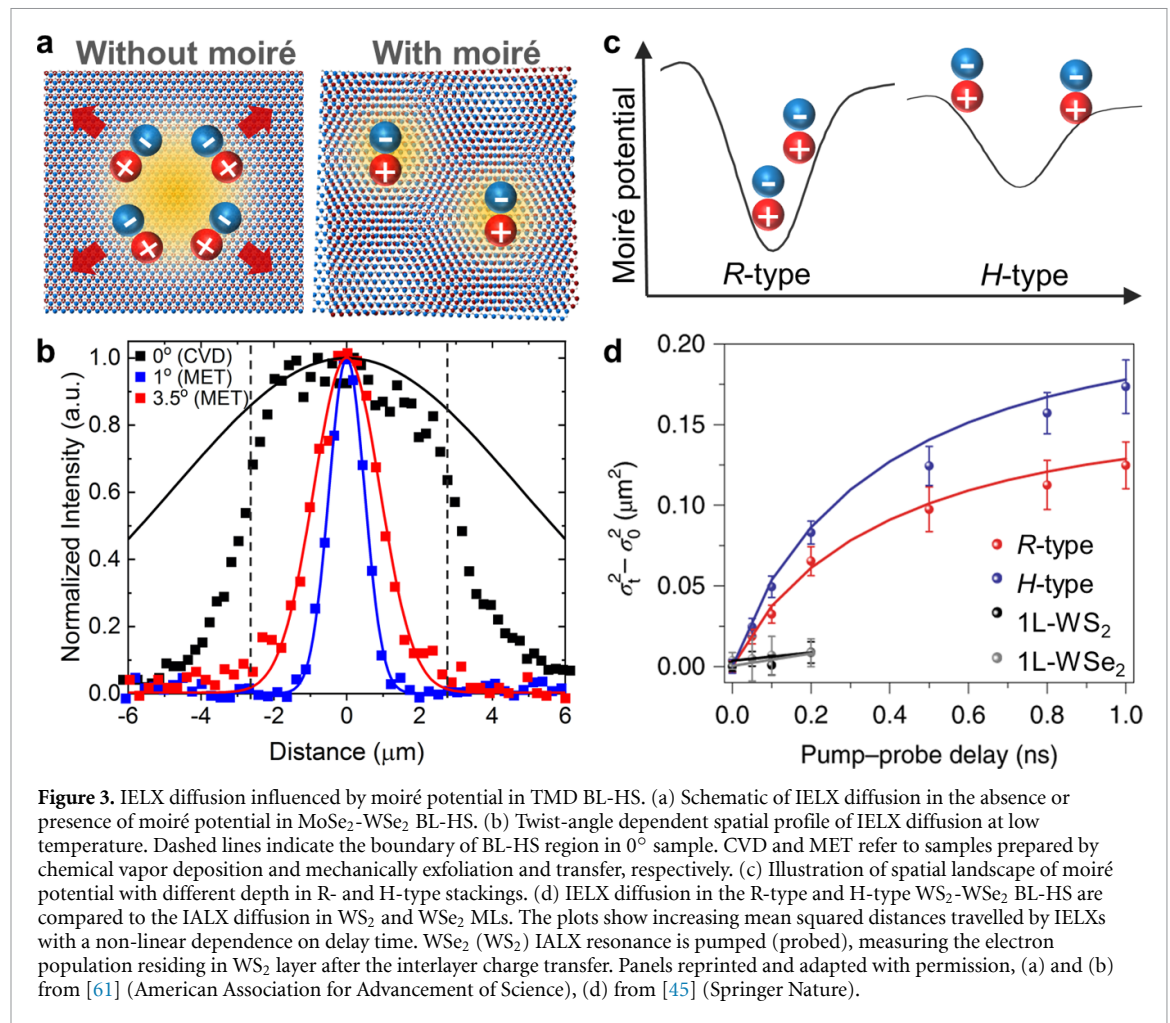
of resonant cavity physics. Further, Li *et al* [51]. report the possibility of interlayer biexciton (IELXX), supported by super-linear excitation power dependence of PL intensity. At the same location within the moiré superlattice, the IELXX energy is 1–5 meV higher than that of the IELX due to the dipolar repulsive interaction. The variation in interaction strength is attributed to the variation in confinement lengths and inter-excitonic distances of the localized IELX [51].

Bai *et al* [47] relates PL signals of MXs to real space imaging of moiré superlattice revealed by piezo force microscopy (PFM). Figure 2(f) shows two distinct PL signals on a MoSe$_2$-WSe$_2$ BL-HS on two different types of moiré superlattice. Type I (figure 2(f) upper panel) is the normal hexagonal moiré superlattice (see inset) whose PL consists of sharp peaks with uniform CP, consistent with earlier results [36, 49]. Type II (figure 2(f) lower panel) is the distorted 1D moiré superlattice (see inset) due to strain, for which the corresponding PL consists of a single broad peak with minimal CP. Interestingly, the broad PL peak from type II moiré superlattice is strongly linearly polarized. The linear polarization direction tends to align with the direction of the primary structure of 1D moiré.

4.3. Singlet and triplet IELXs and other interpretations

A number of optical studies on MoSe$_2$-WSe$_2$ BL-HS report the observation of singlet and triplet IELXs as adjacent peaks with opposite CP in PL measurements [48, 52, 53] (figure 2(g)). The energy separation between these two peaks is about 25–40 meV in agreement with the CB spin splitting of MoSe$_2$. Ciarrocchi *et al* [52] studying R-type BL-HS, assign the double interlayer peaks to singlet (lower energy) and triplet (higher energy) localized at the R_h^X site of the moiré superlattice. For H-type BL-HS, the singlet (higher energy) and triplet (lower energy) are located at H_h^h site [48, 53]. The g-factors are different for IELXs in H-type (∼15.2 for triplet, ∼10.7 for singlet [48]) and in R-type (7.1 ± 1.6 for triplet, −8.5 ± 1.5 for singlet [52]) due to the contribution of spin, and different contribution of angular orbital momentum which depends on where the IELX is localized (R_h^h, R_h^X, or H_h^h) [54, 55]. Singlet and triplet energy positions and intensities are highly tunable (more than 100 meV energy shift) similar to the moiré sharp peaks [49], either by out-of-plane electric field [52] or by electrical doping [48, 52]. More interestingly, since electrical doping can change the relative intensity between singlet and triplet peaks, CP of the IELX emission can be switched from polarization-preserving to polarization-inverting regime [52].

Other studies also report the observation of the double IELX peaks with different interpretations. Hanbicki *et al* [56]. show the emergence of double peaks with opposite CP, and assign the peaks to

Figure 3. IELX diffusion influenced by moiré potential in TMD BL-HS. (a) Schematic of IELX diffusion in the absence or presence of moiré potential in $MoSe_2$-WSe_2 BL-HS. (b) Twist-angle dependent spatial profile of IELX diffusion at low temperature. Dashed lines indicate the boundary of BL-HS region in 0° sample. CVD and MET refer to samples prepared by chemical vapor deposition and mechanically exfoliation and transfer, respectively. (c) Illustration of spatial landscape of moiré potential with different depth in R- and H-type stackings. (d) IELX diffusion in the R-type and H-type WS_2-WSe_2 BL-HS are compared to the IALX diffusion in WS_2 and WSe_2 MLs. The plots show increasing mean squared distances travelled by IELXs with a non-linear dependence on delay time. WSe_2 (WS_2) IALX resonance is pumped (probed), measuring the electron population residing in WS_2 layer after the interlayer charge transfer. Panels reprinted and adapted with permission, (a) and (b) from [61] (American Association for Advancement of Science), (d) from [45] (Springer Nature).

double indirect IELX in momentum space in agreement with density functional theory (DFT) calculations. Miller *et al* [57]. assign the higher (lower) energy peak to momentum direct (indirect) IELX. On the other hand, Calman *et al* [58]. interpret the lower (higher) energy peak as interlayer trion (exciton). Because of these different interpretations, additional experimental techniques and further studies are warranted.

4.4. IELX diffusion

IELX diffusion represents a unique transport problem involving energy, charge and spins in TMD BL-HS [28, 59, 60, 62]. Rivera *et al* have earlier demonstrated that valley-dependent exchange interaction between IELXs of $MoSe_2$-WSe_2 BL-HS in the same valley (K) can cause different repulsive forces for majority-valley (K) and minority valley (K') populations, resulting in valley-asymmetric drift and diffusion of IELXs [28]. The long-lived nature of IELXs in hBN-encapsulated MoS_2-WSe_2 and $MoSe_2$-WSe_2 BL-HS leads to diffusion on the order of a few micrometers, with dynamics manipulation by excitation power or electrical controls [59, 60, 62]. These previous diffusion studies suggest the free-diffusion picture for IELXs in absence of confinement. The absence of

confinement could possibly be due to larger twist-angles or large lattice mismatch resulting in weaker moiré potentials, or from inhomogeneously averaged excitonic response.

Due to the presence of moiré potential, IELX diffusion in incommensurate BL-HS is expected to possess unique features distinct from commensurate BL-HS. While two different views for the IELXs as free or localized carriers exist, recent studies suggest that the presence of moiré potential has a strong influence on IELX diffusion in TMD BL-HS [45, 60, 61, 63]. The moiré potential exhibits periodic energy modulation on the order of $\sim$150 meV, deep enough to completely localize IELXs within the potential or impede their lateral diffusion.

The IELX diffusion in $MoSe_2$-WSe_2 BL-HS with commensurate stacking and corresponding absence of moiré potential, shows the strikingly long diffusion length on the order of a few micrometers, in contrast to the small diffusion lengths in the incommensurate BL-HS and presence of moiré potential (figures 3(a) and (b)) [61]. Moreover, using spatially resolved transient absorption technique, it was observed that the IELX diffusion in WS_2-WSe_2 CVD-grown BL-HS with R-type stacking is suppressed compared to H-type stacking, due to the deeper moiré potential

depth (figures 3(c) and (d)) [45]. To observe the IELX dynamics, WSe_2 (WS_2) IALX resonance is pumped (probed), measuring the electron population residing in WS_2 layer after the interlayer charge transfer. In mechanically stacked $MoSe_2$-WSe_2 BL-HS with near $0°$ stacking, at low optical excitation density, the diffusivity of IELXs can be drastically reduced due to the effective trapping of IELXs by moiré potential. All recent diffusion studies provide a different perspective of spatial diffusion behavior of IELXs in the TMD BL-HS and suggest that the IELX diffusion is dominated by the competition between many-body interactions and localization by moiré potential.

5. Intralayer excitons (IALXs)

Properties of IALXs in a BL-HS can be modified due to the periodic moiré potential operating in the weak or strong-coupling regime. This moiré potential can mix momentum states separated by moiré reciprocal vectors, leading to additional absorption peaks with predicted topological properties, flat exciton dispersion and protection against disorder [11, 19, 37]. Jin *et al* tracked optical reflectance of a WSe_2-WS_2 BL-HS with carrier concentration, and measured three WSe_2 intralayer MX peaks (figure 4(a)) [19]. All peaks blueshift with increasing electron concentration but with varying levels of shift, related to different localization with respect to the moiré superlattice. The peaks vanish with increasing twist-angles signifying the importance of moiré superlattice (inset of figure 4(a)). The twist dependence is in qualitative agreement with calculations performed on a WS_2-MoS_2 BL-HS, considering moiré potentials without any domain formation (figure 4(b)) [37].

The depth of moiré potential for intralayer MXs is relatively small compared to that for interlayer MXs [11]. Similar CP of intralayer $MoSe_2$ MXs (and trions) on a $MoSe_2$-MoS_2 BL-HS and a bare $MoSe_2$ ML has been observed (figure 4(c)) [64]. This work also showed the evolution of IELX and trion peaks to higher and lower energy excitons (X_H, X_L) and trions (T_H, T_L) peaks in the BL-HS. These results suggest unchanged selection rules for IALX (with respect to the IALXs in bare ML) when modulated by the moiré potential, and preservation of rotational symmetry of transitions [11]. Further, the same work [64] measured a small change in $MoSe_2$ trion decay-time from 79 ps in bare ML to 64 ps in the BL-HS for T_H (72 ps for T_L). On the other hand, exciton dynamics are measurement-resolution limited and remain at ~14 ps. However, the modulation depth for intralayer MXs in a $MoSe_2$-MoS_2 BL-HS is ~10 meV [64], whereas for a WSe_2-WS_2 BL-HS is ~30 meV [19]. Thus, in the case of WSe_2-WS_2 BL-HS, varied dynamics may be possible compared to weakly modulating moiré potentials.

The origin of these additional MX peaks is still under vigorous debate. The different additional peaks for the intralayer MX are considered to arise from localization at different high symmetry points in the real-space moiré superlattice. The evidence for these is indirect at best. For example, peak shift of intralayer MX peaks (for WSe_2 exciton in a WSe_2-WS_2 BL-HS) with doping has been attributed to localization of MX peaks, as well as electrons in WS_2 layer, with respect to the moiré superlattice [19]. On the other hand, reconstructed domain related intralayer MX bands have been invoked in a twisted WSe_2 homo BL-HS [65]. The field would benefit with direct nanoscale characterization of structure and optical properties [66].
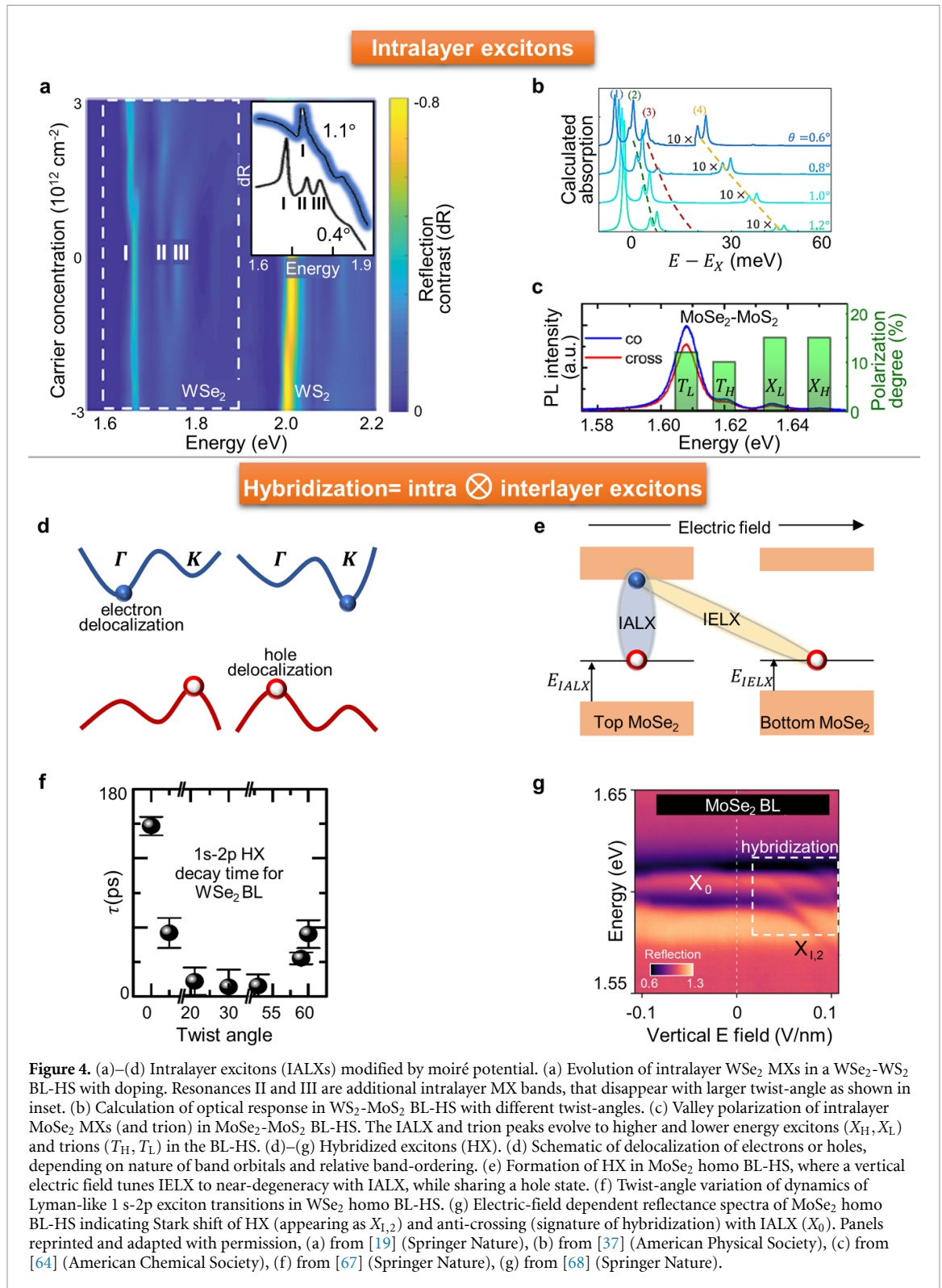
6. Hybridized excitons (HXs)

HXs are created when two conditions are met in a BL-HS: IELX formation due to type-II band alignment, and CB or VB degeneracy between the two layers [41, 67–70]. HXs result from transfer of optical oscillator strength from IALXs to nearly degenerate IELXs and sharing of a common electron or hole state [70]. HXs inherit electric dipole from IELXs and optical dipole from IALXs, and thus, tunable by both electrical and optical fields.

Depending on nature of band orbitals and relative band-ordering, either electrons or holes are delocalized in the two layers (figure 4(d)). For example, in twisted $MoSe_2$ homo BL-HS (for $0°$ stacking), the CB minimum (VB maximum) is located at the K (Γ) momentum-point. Since the orbitals contributing to Γ are more delocalized (compared to K point), the hole is delocalized over the two MLs, whereas the electron is constrained to one of the layers [68]. On the other hand, for twisted WSe_2 homo BL-HS, the electron is delocalized due to CB minima at Γ point[67]. Direct momentum (K–K) IELX were also recently measured in MoS_2 BL-HS, with hybridization controllable by stacking order [70–72]. The picture is slightly more complicated for a hetero BL-HS, where disparate orbital nature of the two component layers must be taken in account.

In a $MoSe_2$-WS_2 BL-HS, CB is nearly degenerate for the two layers, and electron state is shared. Further, the momentum mismatch (Δk, due to twist) is surmountable due to moiré brillouin-zone enabled momentum conservation. The mixing of intralayer moiré bands with IELX states result in enhanced interlayer tunneling and formation of optically-bright HX. This mixing also results in a twist-angle dependence of HX [73], and for Lyman-like (level transitions in an atom) 1s-2p HX transitions (in twisted WSe_2 homo BL-HS [67]).

Due to finite electric dipole, Stark shift of HXs is far stronger than IALXs. In a dual-gated (top and bottom) configuration, both Stark shift of HX and avoided crossing have been observed ($MoSe_2$ homo BL-HS [68], $MoSe_2$-hBN-$MoSe_2$ [41]). Leisgang *et al* observed a large Stark splitting of 120 meV between two degenerate IELX and avoided crossing with the

Figure 4. (a)–(d) Intralayer excitons (IALXs) modified by moiré potential. (a) Evolution of intralayer WSe$_2$ MXs in a WSe$_2$-WS$_2$ BL-HS with doping. Resonances II and III are additional intralayer MX bands, that disappear with larger twist-angle as shown in inset. (b) Calculation of optical response in WS$_2$-MoS$_2$ BL-HS with different twist-angles. (c) Valley polarization of intralayer MoSe$_2$ MXs (and trion) in MoSe$_2$-MoS$_2$ BL-HS. The IALX and trion peaks evolve to higher and lower energy excitons (X_H, X_L) and trions (T_H, T_L) in the BL-HS. (d)–(g) Hybridized excitons (HX). (d) Schematic of delocalization of electrons or holes, depending on nature of band orbitals and relative band-ordering. (e) Formation of HX in MoSe$_2$ homo BL-HS, where a vertical electric field tunes IELX to near-degeneracy with IALX, while sharing a hole state. (f) Twist-angle variation of dynamics of Lyman-like 1 s-2p exciton transitions in WSe$_2$ homo BL-HS. (g) Electric-field dependent reflectance spectra of MoSe$_2$ homo BL-HS indicating Stark shift of HX (appearing as $X_{I,2}$) and anti-crossing (signature of hybridization) with IALX (X_0). Panels reprinted and adapted with permission, (a) from [19] (Springer Nature), (b) from [37] (American Physical Society), (c) from [64] (American Chemical Society), (f) from [67] (Springer Nature), (g) from [68] (Springer Nature).

B-type IALX [72]. Avoided crossing is a characteristic feature of hybridization of resonances, and results from near-degeneracy of electric-field-tuned IELX and nearly unaffected IALX (figures 4(e) and (g)) [68].

Twist-angle can tune the extent of interlayer hybridization, which results in varying temporal dynamics. For 1s-2p HX transitions in twisted WSe$_2$ homo BL-HS, lifetime decreases from 0° to 30° twist-angle followed by an increase till 60° (figure 4(f)) [67]. By increasing the twist-angle beyond 0° (up-to 30°), electron–hole overlap in the same layer increases, leading to reduction in lifetime. Thus, at small (large) twist-angles HX have more interlayer (intralayer) nature and have long (short) lifetimes. With larger twist-angles, interlayer hopping becomes

even weaker, which further reduces the exciton life-time.

7. Strongly correlated electronic states

Following the exciting discoveries in twisted graphene homo BL-HS [23, 74], TMD BL-HS have also been found to possess correlated quantum phenomena revealed by optical spectroscopy and transport measurements [39–41, 75, 76]. Recent theoretical work has shown that the moiré superlattice in TMD BL-HS can be used to simulate the 2D triangular spin-lattice Hubbard model [38]. The model with parameters such as band filling, hopping (t), and on-site repulsive interaction (U), can predict magnetization and correlations. In a TMD moiré superlattice, the realization of a single moiré band with two valley degrees of freedom, playing the role of spins, is useful to simulate this model system. For example, U decreases as the moiré periodicity increases, while t can be modified with choice of component MLs and/or twist angle. Here, the half-filled moiré band can satisfy the condition for strongly correlated states, as the ratio of U to electron bandwidth substantially increases.

Optical spectroscopy coupled with electrical control has been used to investigate strongly correlated electronic phases by probing excitonic resonances. Regan *et al* implement optically-detected resistance and capacitance to measure the carrier concentration in a WSe$_2$-WS$_2$ BL-HS, revealing various doping-dependent insulating states [40]. The induced change in optical contrast (ΔOC) of the WSe$_2$ IALX resonance, under the electrical modulation of the sample's top gate, is directly proportional to the density of states of the moiré superlattice. The ΔOC shows strong gap-like features at $n = n_0/6$, $n_0/3$, and $n_0/2$ hole doping densities, where $n_0/2$ is defined as the density at which one hole occupies one moiré supercell (figure 5(a)). Such gap-like features are enhanced at higher electrical modulation frequency (30 kHz). These insulating states at 1/6 and 1/3 filling of the superlattice are assigned to generalized Wigner crystallization, while Mott insulating state [77, 78] is revealed at one hole per superlattice, arising from Coulomb interaction between holes localized in same moiré superlattice (figure 5(b)). These correlated insulating states are absent in WSe$_2$-WS$_2$ BL-HS with a large twist-angle. Here, we note that the half-filling factor is defined as $n = 1$ in this work [40], while $n_0 = 1/2$ is generally used in other works (and adopted in this review paper).
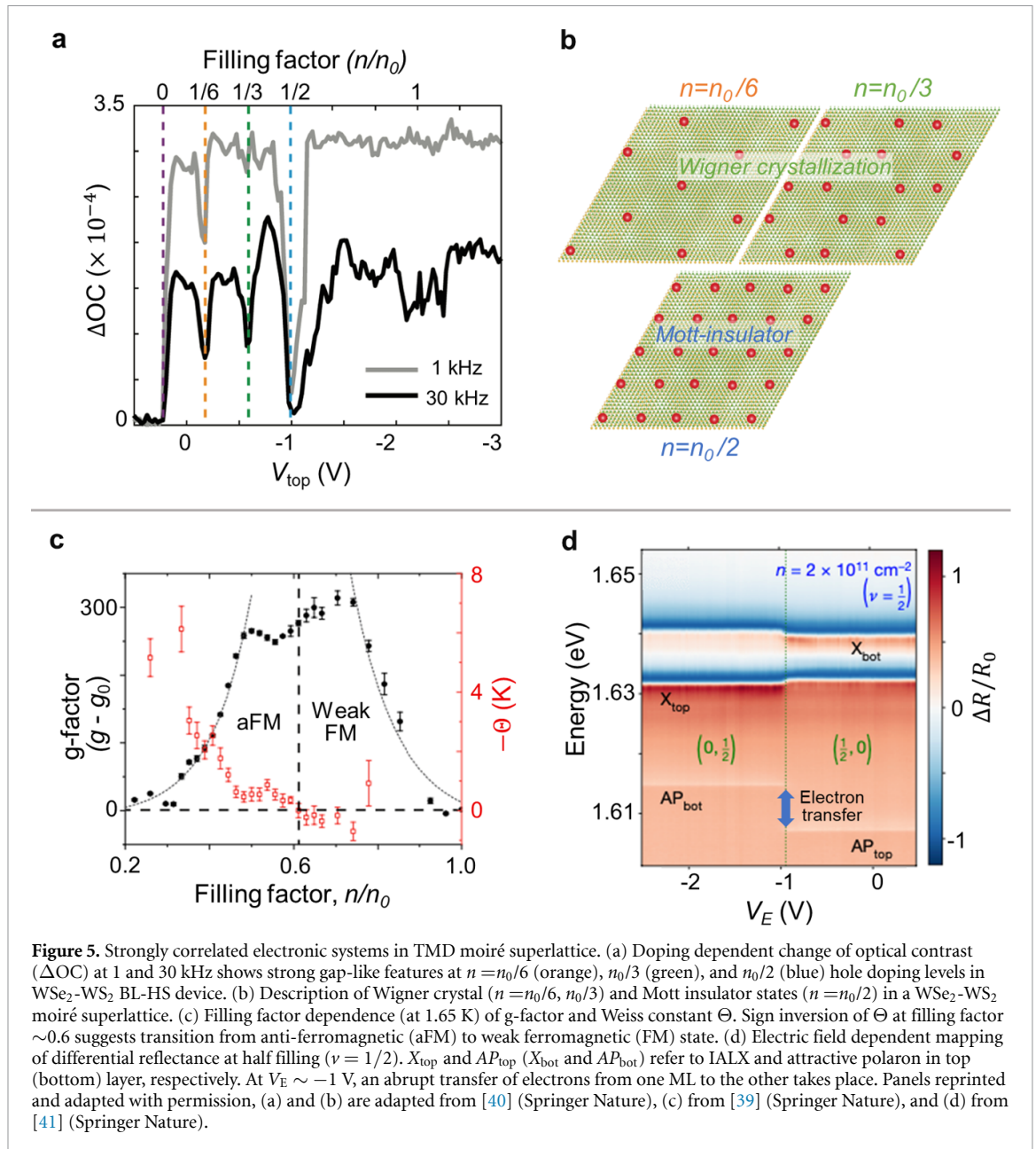
The Hubbard model also predicts different magnetic phases depending on the filling and controlling the interaction regime (U/t) [38, 79–81]. Indeed, a Mott insulating state with antiferromagnetic (aFM) Curie-Weiss behavior was observed at half-filling of WSe$_2$-WS$_2$ moiré superlattice band, while possible signatures of phase-transition from an aFM to a weak FM state were shown above half-filling (figure 5(c))

[39]. Here, the magnetic moments of localized holes are probed using magneto-optical spectroscopy by measuring Zeeman splitting of MX resonances and corresponding g-factors. Particularly, a giant g-factor ($\sim$270) is observed between 0.5 and 0.7 fillings, while a g-factor of -4 (corresponding to IALX of a pristine ML) [54, 55, 82–84] is observed near zero and full fillings. The sensitivity of MXs on magnetic interactions is modeled by a molecular field $\lambda_X M$ (λ_X = coupling constant; M = sample magnetization). The analysis of temperature-dependent magnetic susceptibility χ suggests Curie–Weiss behavior with a negative Weiss-constant (Θ), thus indicating an aFM state in the high U/t regime. Moreover, diverging χ and vanishing Θ near 0.6 filling factor (vertical dashed line in figure 5(c)) represents the possible existence of quantum phase transition from aFM to weak FM state, while the transition temperature was not accessible in this study.

In the context of strongly correlated phases in the Hubbard model, the twisted MoSe$_2$ BL-HS system with insertion of a single layer hBN (between the MoSe$_2$ MLs) has been introduced as a unique regime with long moiré periodicity and suppressed moiré potential [41]. Figure 5(d) shows the vertical external electric field (V_E) dependence of the differential reflectance spectrum ($\Delta R/R_0$) at half-filling of the lowest moiré band. As the electric field increases, an abrupt shift of IALX resonance as well as the complete transfer of oscillator strength between polarons in top and bottom layers (AP_{top} or AP_{bot}) is observed, indicating the complete transfer of all electrons from one MoSe$_2$ ML to the other. This abrupt transfer is indication of an interaction-induced incompressible Mott state in the lowest moiré band. Here the exciton–polaron is a many-body hybrid light matter state, and acts as a spectroscopic tool to measure interactions of excitons and electrons/holes [41].

8. Mapping of moiré potential and reconstruction of domains

So far, we have discussed the effect of moiré potential on opto-electronic properties, without providing direct evidence of moiré superlattice in real space. In this section, we provide real-space nanoscale mapping of rigid moiré superlattices and possibilities of domain reconstruction measured by various techniques including transmission electron microscope (TEM) [19, 68, 85], scanning electron microscopy (SEM) [65, 86], conducting-atomic force microscopy (c-AFM) [21], scanning tunneling microscope (STM) [42, 87] and PFM [47, 88]. In this section, for consistency of nomenclature with the work in this field, we define R_h^h, R_h^X, R_h^M as AA, AB and BA sites respectively (for R, parallel stacking). For H stacking (antiparallel), we define H_h^h, H_h^X, H_h^M as ABBA, AA and BB sites respectively.

Figure 5. Strongly correlated electronic systems in TMD moiré superlattice. (a) Doping dependent change of optical contrast (ΔOC) at 1 and 30 kHz shows strong gap-like features at $n = n_0/6$ (orange), $n_0/3$ (green), and $n_0/2$ (blue) hole doping levels in WSe_2-WS_2 BL-HS device. (b) Description of Wigner crystal ($n = n_0/6$, $n_0/3$) and Mott insulator states ($n = n_0/2$) in a WSe_2-WS_2 moiré superlattice. (c) Filling factor dependence (at 1.65 K) of g-factor and Weiss constant Θ. Sign inversion of Θ at filling factor $\sim$0.6 suggests transition from anti-ferromagnetic (aFM) to weak ferromagnetic (FM) state. (d) Electric field dependent mapping of differential reflectance at half filling ($\nu = 1/2$). X_{top} and AP_{top} (X_{bot} and AP_{bot}) refer to IALX and attractive polaron in top (bottom) layer, respectively. At $V_E \sim -1$ V, an abrupt transfer of electrons from one ML to the other takes place. Panels reprinted and adapted with permission, (a) and (b) are adapted from [40] (Springer Nature), (c) from [39] (Springer Nature), and (d) from [41] (Springer Nature).

For a WSe_2-WS_2 BL-HS (R stacking, twist-angle > 0.3°), moiré unit cell of length 8 nm is observed using annular dark-field scanning TEM (ADF-STEM) (figure 6(a)), consistent with the rigid layer moiré superlattice picture [19]. Earlier high-resolution TEM work also showed the presence of moiré patterns in twisted-MoS_2 layers [89]. STM provides complementary high-resolution spatial mapping of density of states, which in-turn are affected by layer-layer interactions [90]. STM mapping of WSe_2 homo BL-HS (twist-angle $\sim 3°$) shows a moiré period of $\sim$6.3 nm with visible contrast for AA, AB and BA sites (figure 6(b)) [87]. Similar STM work on CVD grown MoS_2-WSe_2 BL-HS (conformal growth, no twist-angle) [42, 91] shows moiré superlattice period of 8.7 nm (figure 6(c)) [91]. In these samples, only the moiré superlattice is observed with no reconstruction (which we explain below).

Structural relaxation of moiré superlattice, at the level of DFT, force-fields or multi-scale modelling of interlayer binding energy densities, reveal that AB (or BA) triangular stacking-domains are energetically favorable compared to AA domains for R stacking (figure 6(d)) [21, 85, 92]. On the other hand, ABBA domains are energetically favorable for H stacking [93, 94]. Thus, energy of the system can be minimized through lattice reconstruction, via expansion of energetically-favorable stacking domains and creation of domain walls. The level of atomic reconstruction is related to two competing parameters: interlayer stacking energy, which drives atomic reconstruction; and intralayer strain, which opposes reconstruction. In simpler terms, interlayer stacking energy drives domain formation (and stretching of layers to form commensurate structure), whereas the intralayer bonding aims

Figure 6. Rigid moiré superlattice (a)–(c). (a) WSe$_2$-WS$_2$ BL-HS (annular dark-field scanning transmission electron microscopy (ADF-STEM), R-type stacking, ∼0° twist-angle). (b) WSe$_2$ homo BL-HS (scanning tunneling microscopy (STM), R, ∼3°). (c) CVD grown MoS$_2$-WSe$_2$ BL-HS (STM, R, 0°). Reconstruction and domains (d)–(j). (d) Calculation of stacking energy for energetically favorable AB and BA domains for R stacking. Reconstructed domains observed in (e) WSe$_2$ homo BL-HS (piezo-force microscopy (PFM), R, ∼0°) and (f) MoSe$_2$ homo BL-HS (tilted-dark-field TEM, R, ∼0°). (g) Calculated reconstructed domains for H stacking. Reconstructed distorted hexagonal domains observed in (h) MoS$_2$ homo BL-HS (ADF-STEM, H stacking, 0.25°); (i) WSe$_2$-MoSe$_2$ BL-HS (conducting atomic force microscopy (c-AFM), H, ∼0°) and (j) summary of variation of critical twist-angle (θ_c) with various HS component and processing relevant properties. Panels reprinted and adapted with permission, (a) from [19] (Springer Nature), (b) from [87] (Springer Nature), (c) from [91] (American Chemical Society), (d) and (i) from [21] (American Chemical Society), (e) from [88] (Springer Nature), (f) from [68], (g) from [94] (American Physical Society), and (h) from [85] (Springer Nature).

to maintain pristine, rigid lattice. Below a critical twist-angle (θ_c), potential energy gradient due to interlayer stacking energy can dominate the restoring force due to intralayer strain, and can result in reconstruction [88].

For R stacked BL-HS with small twist-angles, significant lattice reconstruction has been observed (WS$_2$-MoS$_2$ BL-HS, 1.5° twist-angle) by using ADF-STEM [85]. Reconstructed domains in WSe$_2$ homo BL-HS were measured using PFM (figure 6(e)), where contrast results from modulation of piezoelectric tensor by moiré superlattice potential or reconstructed domains [47, 88]. Further, inversion symmetry of AB and BA domains can be broken by explicit

tilting of the sample in DF-TEM, thus enabling direct domain visualization in twisted MoSe$_2$ (∼0°) homo BL-HS (figure 6(f)) [68]. DF-TEM uses an aperture to filter a particular Bragg diffracted peak, thus providing a direct mapping of stacking order [95, 96]. Similarly, tilted-SEM has measured varying sizes of domains in WSe$_2$ homo BL-HS (∼0°) while differentiating between AB and BA domains, and is an encouraging new technique due to its compatibility with hBN encapsulated BL-HS prepared for optical experiments [65, 86]. For increasing twist-angle, it has been observed (via TEM) that triangular domain contrast is weakened and becomes close to one-directional fringes, a characteristic of simple

rotational moiré structure without reconstruction [21, 95].

For H stacking, distorted hexagonal domains (ABBA) are energetically-favorable (figure 6(g)) [85, 92, 94], but θ_c is much smaller compared to the case of R stacking. For MoS_2 homo BL-HS (H stacking, 0.25°), distorted hexagonal domains (with varying size) were observed using ADF-STEM (figure 6(h)) [85]. Similarly, c-AFM measured reconstruction in WSe_2-$MoSe_2$ BL-HS (H stacking, ~0°) (figure 6(i)) [21].

It is important to remember that the calculations shown in figures 6(d) and (g) are thermodynamic equilibrium calculations. Driving forces are needed to ascend possible thermodynamic barriers and force the system towards equilibrium, even for twist-angles $< \theta_C$. Possible driving forces are thermal annealing process or mechanical inputs (for example, shear) usually present during HS preparation. On the other hand, hBN encapsulation can change the amount of reconstruction by providing opposing driving forces, as shown explicitly for the case of graphene-hBN [90], and hinted at for WSe_2 homo BL-HS [87]. For materials with similar unit cell size ($MoSe_2$-WSe_2, or homo-BLs), θ_c is much larger compared to materials with significant lattice mismatch (example MoS_2-WSe_2). We summarize some of these ideas in the figure 6(j). Thus, for low lattice mismatch, R stacking, no encapsulation, or high processing temperature, θ_C should be large.

9. Conclusion and outlook

In this review paper, we have reviewed the state of the twistronics field focusing on TMD BL-HS. We have discussed moiré IELXs and IALXs and their hybridization, effect of moiré superlattice on diffusion, strongly correlated states, and moiré superlattice mapping. Tremendous progress has been made in the past few years, which has opened many avenues of research as well as raised fundamental questions about origin of spectral features.

Moiré IELXs promise to be new sources of 2D-array of identical quantum emitters, with applications in optoelectronic devices, and quantum communication. These quantum emitters are highly tunable by various experimental knobs, including vertical electric field [49, 52], doping [52], and strain [47]. Moiré IELX dipole can point in or out-of-plane, depending on whether exciton is of spin-singlet or triplet nature, and on exciton location within the moiré superlattice [24]. IELX diffusion is also affected by the moiré potential, with different diffusion regimes for R and H-type stacking. An IELX dipole is thus tunable for energy, polarization and strength using existing opto-electronic means, and thus relevant for opto-electronic applications.

IALXs are also modified by the moiré potential, with the twist-angle directly tuning the energy spacing and oscillator strength of additional resonances. An outstanding question is how the dynamics of IALXs are affected by the strength of the moiré potential. Similar questions arise for HXs, with the additional complication of momentum space band-ordering. Since HXs are tunable by both optical and electrical fields, they offer promise in integrated photonics as active materials [4], as well as in fundamental measurements of cavity-coupling dynamics. Topological properties and presence of flat bands (in twisted homo BL-HS) are also exciting fields of research and we encourage extensive theoretical and experimental work.

TMD BL-HS represents a promising solid-state platform to simulate triangular-lattice Hubbard models based on moiré superlattice. Feature-rich strongly correlated physics can be explored by combination of optical spectroscopy and electrical measurements for TMD BL-HS. Moiré potential depth in different BL-HS offers modulation of Hubbard model tuning parameters and corresponding modulation of correlations. The physics of moiré-systems with low filling factors remains to be explored, requiring work to prepare low resistance contacts and low carrier concentration samples.

For a meaningful comparison of theory and experiment regarding MXs, direct nanoscale optical mapping techniques are sorely needed. With large spatial resolution ($\sim\mu$m) of far-field optics, evidence for MXs are often reported with conflicting data and interpretations. Near-field optical techniques such as cathodoluminescence [66] and tip-enhanced PL [97–99] offer the possibility of mapping of individual moiré supercells with spatial resolution of a few nanometers. Cathodoluminescence in a TEM has the added advantage of direct optical-structural correspondence, and simultaneous measurement of stacking order. Such techniques can naturally lead to measurement of effects of strain and atomic scale defects.

Mapping techniques (PFM, TEM, STEM, and STM) have established the presence of rigid moiré superlattice in BL-HS, with evolution to reconstructed domains for small twist-angles and low lattice mismatch. Since evidence of reconstruction is growing, the field now needs to look at the processing conditions more carefully with systematic studies critically needed. A concern is the varying size of reconstructed domains across micrometer length scales, most probably resulting from pinning at defect sites or imperfections, which naturally lead to spatially varying opto-electronic properties. Further, how reconstruction changes the optical properties of TMD BL-HS and whether novel physical states can be created, are outstanding topics for investigation [85]. Interesting avenues of research will be as to how the moiré picture is modified in reconstructed domains.

Acknowledgments

Author contributions

All authors contributed to writing of the review paper.

Conflict of interest

The authors declare no competing interests

ORCID iDs

Junho Choi ⓘ https://orcid.org/0000-0002-8740-650X
Akshay Singh ⓘ https://orcid.org/0000-0003-1059-065X

References

[1] Dong R and Kuljanishvili I 2017 Review article: progress in fabrication of transition metal dichalcogenides heterostructure systems *J. Vac. Sci. Technol.* B **35** 030803

[2] Rivera P *et al* 2018 Interlayer valley excitons in heterobilayers of transition metal dichalcogenides *Nat. Nanotech.* **13** 1004–15

[3] Li M-Y, Chen C-H, Shi Y and Li L-J 2016 Heterostructures based on two-dimensional layered materials and their potential applications *Mater. Today* **19** 322–35

[4] Singh A *et al* 2020 Refractive uses of layered and two-dimensional materials for integrated photonics *ACS Photonics* **7** 3270–85

[5] Liu Y *et al* 2016 Van der Waals heterostructures and devices *Nat. Rev. Mater.* **1** 16042

[6] Mlack J T *et al* 2017 Transfer of monolayer TMD WS2 and Raman study of substrate effects *Sci. Rep.* **7** 43037

[7] Gurarslan A *et al* 2014 Surface-energy-assisted perfect transfer of centimeter-scale monolayer and few-layer MoS2 films onto arbitrary substrates *ACS Nano* **8** 11522–8

[8] Arute F *et al* 2019 Quantum supremacy using a programmable superconducting processor *Nature* **574** 505–10

[9] Vaziri S *et al* 2019 Ultrahigh thermal isolation across heterogeneously layered two-dimensional materials *Sci. Adv.* **5** eaax1325

[10] Ribeiro-Palau R *et al* 2018 Twistable electronics with dynamically rotatable heterostructures *Science* **361** 690

[11] Yu H, Liu G-B, Tang J, Xu X and Yao W 2017 Moiré excitons: from programmable quantum emitter arrays to spin-orbit–coupled artificial lattices *Sci. Adv.* **3** e1701696

[12] Gillen R and Maultzsch J 2018 Interlayer excitons in MoSe$_2$/WSe$_2$ heterostructures from first principles *Phys. Rev.* B **97** 165306

[13] Hsu W-T *et al* 2018 Negative circular polarization emissions from WSe$_2$/MoSe$_2$ commensurate heterobilayers *Nat. Commun.* **9** 1356

[14] Castellanos-Gomez A *et al* 2014 Deterministic transfer of two-dimensional materials by all-dry viscoelastic stamping *2D Mater.* **1** 011002

[15] Kim K *et al* 2016 van der Waals heterostructures with high accuracy rotational alignment *Nano Lett.* **16** 1989–95

[16] Chakraborty C, Vamivakas N and Englund D 2019 Advances in quantum light emission from 2D materials *Nanophotonics* **8** 2017–32

[17] Liao W, Huang Y, Wang H and Zhang H 2019 Van der Waals heterostructures for optoelectronics: progress and prospects *Appl. Mater. Today* **16** 435–55

[18] Tran K *et al* 2017 Disorder-dependent valley properties in monolayer WSe$_2$ *Phys. Rev.* B **96** 041302

[19] Jin C *et al* 2019 Observation of moiré excitons in WSe2/WS2 heterostructure superlattices *Nature* **567** 76–80

[20] Tran K *et al* 2019 Evidence for moiré excitons in van der Waals heterostructures *Nature* **567** 71–75

[21] Rosenberger M R *et al* 2020 Twist angle-dependent atomic reconstruction and moiré patterns in transition metal dichalcogenide heterostructures *ACS Nano* **14** 4550–8

[22] Liao M *et al* 2020 Precise control of the interlayer twist angle in large scale MoS2 homostructures *Nat. Commun.* **11** 2153

[23] Cao Y *et al* 2018 Unconventional superconductivity in magic-angle graphene superlattices *Nature* **556** 43–50

[24] Yu H, Liu G-B and Yao W 2018 Brightened spin-triplet interlayer excitons and optical selection rules in van der Waals heterobilayers *2D Mater.* **5** 035021

[25] Kang J, Tongay S, Zhou J, Li J and Wu J 2013 Band offsets and heterostructures of two-dimensional semiconductors *Appl. Phys. Lett.* **102** 012111

[26] Rivera P *et al* 2015 Observation of long-lived interlayer excitons in monolayer MoSe$_2$–WSe$_2$ heterostructures *Nat. Commun.* **6** 6242

[27] Gong Y *et al* 2014 Vertical and in-plane heterostructures from WS$_2$/MoS$_2$ monolayers *Nat. Mater.* **13** 1135–42

[28] Rivera P *et al* 2016 Valley-polarized exciton dynamics in a 2D semiconductor heterostructure *Science* **351** 688

[29] Jin C *et al* 2017 On optical dipole moment and radiative recombination lifetime of excitons in WSe2 *Adv. Funct. Mater.* **27** 1601741

[30] Wang H *et al* 2016 Radiative lifetimes of excitons and trions in monolayers of the metal dichalcogenide MoS$_2$ *Phys. Rev.* B **93** 045407

[31] Yu H, Wang Y, Tong Q, Xu X and Yao W 2015 Anomalous light cones and valley optical selection rules of interlayer excitons in twisted heterobilayers *Phys. Rev. Lett.* **115** 187002

[32] Nayak P K *et al* 2017 Probing evolution of twist-angle-dependent interlayer excitons in MoSe$_2$/WSe$_2$ van der Waals heterostructures *ACS Nano* **11** 4041–50

[33] Kunstmann J *et al* 2018 Momentum-space indirect interlayer excitons in transition-metal dichalcogenide van der Waals heterostructures *Nat. Phys.* **14** 801–5

[34] Choi J *et al* 2020 Twist angle dependent interlayer exciton lifetimes in van der Waals heterostructures (arXiv:2007.15196)

[35] Wu F, Lovorn T and MacDonald A H 2018 Theory of optical absorption by interlayer excitons in transition metal dichalcogenide heterobilayers *Phys. Rev.* B **97** 035306

[36] Seyler K L *et al* 2019 Signatures of moiré-trapped valley excitons in MoSe2/WSe2 heterobilayers *Nature* **567** 66–70

[37] Wu F, Lovorn T and MacDonald A H 2017 Topological exciton bands in moiré heterojunctions *Phys. Rev. Lett.* **118** 147401

[38] Wu F, Lovorn T, Tutuc E and MacDonald A H 2018 Hubbard model physics in transition metal dichalcogenide moiré bands *Phys. Rev. Lett.* **121** 026402

[39] Tang Y *et al* 2020 Simulation of Hubbard model physics in WSe2/WS2 moiré superlattices *Nature* **579** 353–8

[40] Regan E C *et al* 2020 Mott and generalized Wigner crystal states in WSe2/WS2 moiré superlattices *Nature* **579** 359–63

[41] Shimazaki Y *et al* 2020 Strongly correlated electrons and hybrid excitons in a moiré heterostructure *Nature* **580** 472–7

[42] Zhang C *et al* 2017 Interlayer couplings, moiré patterns, and 2D electronic superlattices in MoS_2/WSe_2 hetero-bilayers *Sci. Adv.* **3** e1601459

[43] Lu X, Li X and Yang L 2019 Modulated interlayer exciton properties in a two-dimensional moiré crystal *Phys. Rev. B* **100** 155416

[44] Brem S, Linderälv C, Erhart P and Malic E 2020 Tunable phases of moiré excitons in van der Waals heterostructures *Nano Lett.* **20** 8534–8540

[45] Yuan L *et al* 2020 Twist-angle-dependent interlayer exciton diffusion in WS_2–WSe_2 heterobilayers *Nat. Mater.* **19** 617–23

[46] Jin C *et al* 2019 Identification of spin, valley and moiré quasi-angular momentum of interlayer excitons *Nat. Phys.* **15** 1140–4

[47] Bai Y *et al* 2020 Excitons in strain-induced one-dimensional moiré potentials at transition metal dichalcogenide heterojunctions *Nat. Mater.* **19** 1068–73

[48] Wang T *et al* 2020 Giant valley-zeeman splitting from spin-singlet and spin-triplet interlayer excitons in WSe_2/$MoSe_2$ heterostructure *Nano Lett.* **20** 694–700

[49] Baek H, Brotons-Gisbert M, Koong Z X, Campbell A, Rambach M, Watanabe K, Taniguchi T and Gerardot B D 2020 Highly energy-tunable quantum light from moiré-trapped excitons *Sci. Adv.* **6** eaba8526

[50] Brotons-Gisbert M *et al* 2020 Spin–layer locking of interlayer excitons trapped in moiré potentials *Nat. Mater.* **19** 630–6

[51] Li W, Lu X, Dubey S, Devenica L and Srivastava A 2020 Dipolar interactions between localized interlayer excitons in van der Waals heterostructures *Nat. Mater.* **19** 624–9

[52] Ciarrocchi A *et al* 2019 Polarization switching and electrical control of interlayer excitons in two-dimensional van der Waals heterostructures *Nat. Photon.* **13** 131–6

[53] Zhang L *et al* 2019 Highly valley-polarized singlet and triplet interlayer excitons in van der Waals heterostructure *Phys. Rev. B* **100** 041402

[54] Woźniak T, Faria Junior P E, Seifert G, Chaves A and Kunstmann J 2020 Exciton *g* factors of van der Waals heterostructures from first-principles calculations *Phys. Rev. B* **101** 235408

[55] Xuan F and Quek S Y 2020 Valley Zeeman effect and Landau levels in two-dimensional transition metal dichalcogenides *Phys. Rev. Res.* **2** 033256

[56] Hanbicki A T *et al* 2018 Double indirect interlayer exciton in a $MoSe_2$/WSe_2 van der Waals heterostructure *ACS Nano* **12** 4719–26

[57] Miller B *et al* 2017 Long-lived direct and indirect interlayer excitons in van der Waals heterostructures *Nano Lett.* **17** 5229–37

[58] Calman E V *et al* 2020 Indirect excitons and trions in $MoSe_2$/WSe_2 van der Waals heterostructures *Nano Lett.* **20** 1869–75

[59] Unuchek D *et al* 2018 Room-temperature electrical control of exciton flux in a van der Waals heterostructure *Nature* **560** 340–4

[60] Unuchek D *et al* 2019 Valley-polarized exciton currents in a van der Waals heterostructure *Nat. Nanotech.* **14** 1104–9

[61] Choi J *et al* 2019 Moiré potential impedes interlayer exciton diffusion in van der Waals heterostructures *Sci. Adv.* **6** eaba8866

[62] Jauregui L A *et al* 2019 Electrical control of interlayer exciton dynamics in atomically thin heterostructures *Science* **366** 870

[63] Wang J *et al* 2020 Diffusivity reveals three distinct phases of interlayer excitons in $MoSe_2$/WSe_2 heterobilayers (arXiv:2001.03812)

[64] Zhang N *et al* 2018 Moiré intralayer excitons in a $MoSe_2$/MoS_2 heterostructure *Nano Lett.* **18** 7651–7

[65] Andersen T I *et al* 2019 Moiré excitons correlated with superlattice structure in twisted WSe_2/WSe_2 homobilayers (arXiv:1912.06955)

[66] Singh A, Lee H Y and Gradečak S 2020 Direct optical-structure correlation in atomically thin dichalcogenides and heterostructures *Nano Res.* **13** 1363–8

[67] Merkl P *et al* 2020 Twist-tailoring Coulomb correlations in van der Waals homobilayers *Nat. Commun.* **11** 2167

[68] Sung J *et al* 2020 Broken mirror symmetry in excitonic response of reconstructed domains in twisted $MoSe_2$/$MoSe_2$ bilayers *Nat. Nanotech.* **15** 750–4

[69] Brem S *et al* 2020 Hybridized intervalley moiré excitons and flat bands in twisted WSe_2 bilayers *Nanoscale* **12** 11088–94

[70] Hsu W-T *et al* 2019 Tailoring excitonic states of van der Waals bilayers through stacking configuration, band alignment, and valley spin *Sci. Adv.* **5** eaax7407

[71] Paradisanos I *et al* 2020 Controlling interlayer excitons in MoS_2 layers grown by chemical vapor deposition *Nat. Commun.* **11** 2391

[72] Leisgang N *et al* 2020 Giant Stark splitting of an exciton in bilayer MoS_2 *Nat. Nanotech.* **15** 901–7

[73] Alexeev E M *et al* 2019 Resonantly hybridized excitons in moiré superlattices in van der Waals heterostructures *Nature* **567** 81–86

[74] Cao Y *et al* 2018 Correlated insulator behaviour at half-filling in magic-angle graphene superlattices *Nature* **556** 80–84

[75] Xu Y *et al* 2020 Correlated insulating states at fractional fillings of moiré superlattices *Nature* **587** 214–8

[76] Wang L *et al* 2020 Correlated electronic phases in twisted bilayer transition metal dichalcogenides *Nat. Mater.* **19** 861–6

[77] Mott N F 1990 *Metal-Insulator Transitions* 2nd edn (London: Taylor & Francis) 0-85066-783-6

[78] Imada M, Fujimori A and Tokura Y 1998 Metal-insulator transitions *Rev. Mod. Phys.* **70** 1039–263

[79] Merino J, Powell B J and McKenzie R H 2006 Ferromagnetism, paramagnetism, and a Curie-Weiss metal in an electron-doped Hubbard model on a triangular lattice *Phys. Rev. B* **73** 235107

[80] Zheng W, Singh R R P, McKenzie R H and Coldea R 2005 Temperature dependence of the magnetic susceptibility for triangular-lattice antiferromagnets with spatially anisotropic exchange constants *Phys. Rev. B* **71** 134422

[81] Rohringer G *et al* 2018 Diagrammatic routes to nonlocal correlations beyond dynamical mean field theory *Rev. Mod. Phys.* **90** 025003

[82] Koperski M *et al* 2018 Orbital, spin and valley contributions to Zeeman splitting of excitonic resonances in $MoSe_2$, WSe_2 and WS_2 Monolayers *2D Mater.* **6** 015001

[83] Deilmann T, Krüger P and Rohlfing M 2020 *Ab initio* studies of exciton *g* factors: monolayer transition metal dichalcogenides in magnetic fields *Phys. Rev. Lett.* **124** 226402

[84] Förste J *et al* 2020 Exciton g-factors in monolayer and bilayer WSe_2 from experiment and theory (*Nat. Comm.*) **11** 4539

[85] Weston A *et al* 2020 Atomic reconstruction in twisted bilayers of transition metal dichalcogenides *Nat. Nanotech.* **15** 592–7

[86] Sushko A *et al* 2019 High resolution imaging of reconstructed domains and moire patterns in functional van der Waals heterostructure devices (arXiv:1912.07446)

[87] Zhang Z *et al* 2020 Flat bands in small angle twisted bilayer WSe_2 *Nat. Phys.* **16** 1093–6

[88] McGilly L J *et al* 2019 Visualization of moiré superlattices *Nat. Nanotech.* **15** 580–4

[89] Reyes-Gasga J, Tehuacanero S and Yacamán M J 1998 Moiré patterns in high resolution electron microscopy images of MoS_2 *Microsc. Res. Tech.* **40** 2–9

[90] Woods C R *et al* 2014 Commensurate–incommensurate transition in graphene on hexagonal boron nitride *Nat. Phys.* **10** 451–6

[91] Pan Y *et al* 2018 Quantum-confined electronic states arising from the moiré pattern of MoS_2–WSe_2 heterobilayers *Nano Lett.* **18** 1849–55

[92] Naik M H, Maity I, Maiti P K and Jain M 2019 Kolmogorov–crespi potential for multilayer transition-metal dichalcogenides: capturing structural transformations in moiré superlattices *J. Phys. Chem. C* **123** 9770–8

[93] Maity I, Maiti P K, Krishnamurthy H R and Jain M 2019 Reconstruction of moiré lattices in twisted transition metal dichalcogenide bilayers (arXiv:1912.08702)

[94] Maity I, Naik M H, Maiti P K, Krishnamurthy H R and Jain M 2020 Phonons in twisted transition-metal dichalcogenide bilayers: ultrasoft phasons and a transition from a superlubric to a pinned phase *Phys. Rev. Res.* **2** 013335

[95] Yoo H *et al* 2019 Atomic and electronic reconstruction at the van der Waals interface in twisted bilayer graphene *Nat. Mater.* **18** 448–53

[96] Brown L *et al* 2012 Twinning and twisting of tri- and bilayer graphene *Nano Lett.* **12** 1609–15

[97] Park K-D, Jiang T, Clark G, Xu X and Raschke M B 2018 Radiative control of dark excitons at room temperature by nano-optical antenna-tip Purcell effect *Nat. Nanotech.* **13** 59–64

[98] Okuno Y *et al* 2018 Probing the nanoscale light emission properties of a CVD-grown MoS2 monolayer by tip-enhanced photoluminescence *Nanoscale* **10** 14055–9

[99] Su W, Kumar N, Mignuzzi S, Crain J and Roy D 2016 Nanoscale mapping of excitonic processes in single-layer MoS2 using tip-enhanced photoluminescence microscopy *Nanoscale* **8** 10564–9